Communication

Intermediate phases in sodium intercalation into MoS_2 nanosheets and their implications for sodium-ion batteries

Qianqian Li[a,b,1], Zhenpeng Yao[a,1], Jinsong Wu[a,b,*,1], Sagar Mitra[c], Shiqiang Hao[a], Tuhin Subhra Sahu[c], Yuan Li[a,b], Chris Wolverton[a], Vinayak P. Dravid[a,b,*]

[a] Department of Materials Science and Engineering, Northwestern University, Evanston, IL 60208, USA
[b] The NUANCE Center, Northwestern University, Evanston, IL 60208, USA
[c] Department of Energy Science and Engineering, Indian Institute of Technology Bombay, Powai, Mumbai 400076, India

ARTICLE INFO

ABSTRACT

Alkali metal ion intercalation into layered transition-metal dichalcogenide structures is a promising approach to make next generation rechargeable batteries for energy storage. It has been noted that the number of Na-ions which can be reversibly intercalated and extracted per MoS_2 is limited, and the chemical and electrochemical processes/mechanisms remain largely unknown, especially for nano-sized materials. Here, sodiation of MoS_2 nanosheets are studied by in-situ electron diffraction and the phase transformations in sodiation are identified with the aid of DFT calculations to reveal the reaction mechanism. Several thermodynamically stable/metastable structures are identified in the sodiation pathway of MoS_2 nanosheets, previously unnoticed in bulk MoS_2. The gradual reduction of Mo^{4+} upon Na-ion intercalation leads to a transition of the Mo-S polyhedron from a trigonal prism to an octahedron around 0.375 Na per MoS_2 inserted (i.e. $Na_{0.375}MoS_2$). When the intercalated Na-content is larger than 1.75 per MoS_2 structural unit (i.e. $Na_{1.75}MoS_2$), the MoS_2 layered structure collapses and the intercalation reaction is replaced by an irreversible conversion reaction with the formation of Na_2S and metal Mo nanoparticles. The calculated sodiation pathways reproduce the experimental sodiation voltages. The current observations provide useful insights in developing sodium-ion batteries with high cycling stability.

1. Introduction

To meet the demand of inexpensive and environmentally friendly energy storage technologies, sodium-ion batteries are promising especially for large-scale energy storage integrated with renewable energy sources such as solar and wind. Due to the scarcity of lithium, there are clear and compelling economic and practical drivers to explore alternatives to lithium ions in charge storage devices. Sodium-ion batteries have many advantages due to the intrinsic advantages of sodium, e.g., it is environmentally benign, ease to recover, and has lower cost and relative abundance [1,2]. If sodium ion batteries can be a commercial substitute for lithium ion batteries in daily life, the cost could be reduced by nearly 30%, while ensuring greater sustainability [3]. In addition, water-based electrolytes might be developed in Na-ion batteries, due to the higher half-reaction potential for sodium relative to lithium. The low voltage operation would make Na-ion cells cheaper by using water-based electrolytes to replace organic ones, which makes a pathway towards developing environmentally benign batteries [4].

There are, however, disadvantages of sodium-ion batteries, such as poor cycling stability and low rate capability of existing anodes, and lower energy densities. These disadvantages prevent sodium ion batteries from practical applications, which imposes urgency in research to develop more efficient electrode materials for sodium-ion batteries.

Transition-metal dichalcogenide materials such as molybdenum disulfide (MoS_2) have layered structures in which each layer has a slab of transition metal atoms sandwiched by two slabs of chalcogenide atoms. They are potentially promising electrodes materials for alkali- and alkaline-earth-ion rechargeable batteries, such as Li^+ [5–10], Na^+ [11], Mg^{2+} [12], and even K^+ [13]. Covalent bonds are formed between Mo and S within each layer and the Mo-S polyhedron can be described as a trigonal prism where Mo^{4+} is in the center of the prism. In the structure, adjacent MoS_2 layers are interconnected with weak van der Waals forces, and there is enough space between the layers to host alkali metal ions during charge. MoS_2 allows alkali ions to intercalate therein without a significant volume expansion [14], which suggests the

possibility of MoS_2 as a potential electrode material for high capacity rechargeable batteries [5,15,16]. However, the number of the alkali cations which can be hosted in the S-Mo-S layer is limited by the structural stability of the framework. It has been shown that up to 1.5 cations can be stored per formula unit of MoS_2 before the layered structure collapses [17]. Additionally, a structural transition between trigonal 2H- and octahedral $1T-AMoS_2$ (A = Li, Na, K, et al.) accompanied by an electronic structure change from semiconducting to metallic has been observed upon intercalation of alkali-metal ions [11,17–21]. The phase transformation from 2 H to 1 T involves a transversal gliding of one S plane [20,22] and it has been further confirmed by the electron diffraction patterns (EDP) [8,9]. Sodium intercalation into MoS_2 has resulted in several Na-intercalated phases, such as $2H-MoS_2$ (a = 0.316 nm and c = 1.229 nm), $2H-Na_{0.5}MoS_2$ (P1; a = 0.321 nm and c = 1.506 nm), $1T-Na_{0.5}MoS_2$ (P2; a= 0.306 nm and c = 1.397 nm), $1T-NaMoS_2$ (P3; a = 0.311 nm and c = 1.429 nm) and Na_xS (P4; a = 0.343 nm and c=1.397 nm). These phases have been identified by *ex-situ* X-ray and electron microscopy.

The phase transformations and reaction pathways involved in electrode materials during charge and discharge are often quite complex, and can involve both thermodynamically stable and metastable processes. Recent developments in *in-situ* high-resolution transmission electron microscopy (TEM) have shown it as a unique tool to conduct real time structural and morphological measurements in electrochemical reaction processes [23–33]. Hence, *in-situ* TEM makes it possible to analyze stable/metastable processes which occur during sodiation in electrode materials which have been dynamically charged/discharged. *In-situ* high-resolution TEM has been previously applied to study the dynamics of Na transport in MoS_2 nanostructure and reveals a two-phase reaction mechanism [11]. In general, a large electron beam dose is required to imaging the structure at atomic resolution, which introduces the possibility of artificial microstructural changes in observation. As a complementary, efficient tool, density

functional theory (DFT) calculations have been widely used to accurately reveal the detailed underlying mechanisms that are often difficult to obtain solely *via* experiments [34–37]. Here, we applied *in-situ* electron diffraction with a quite low electron beam dose combined with DFT calculations to study the dynamically structural evolution of sodium-intercalated MoS_2 crystals during sodiation. By carefully indexing the diffraction patterns and compared to the DFT calculations, we identified a series of intermediate phases with the sodium accommodation maximum determined and the 2H/1T phase transformation composition clarified.

2. Material and methods

2.1. Synthesis of MoS_2 materials

All chemicals were purchased from Sigma Aldrich and used as received without any further purification. MoS_2 nanosheets were prepared by liquid phase exfoliation of commercially available MoS_2 (Aldrich) powder *via* sonication treatment using water/isopropyl alcohol (IPA) as mixed solvents. Typically, 100 mg of MoS_2 powder was dispersed into 30 mL of water/IPA (40%) mixture, which then sonicated (250 W Branson Ultrasonifier, 35% amplitude, Pulse on: 15 s, Pulse off: 2 s) for 5 h. Now the dispersion was left for 1 week to allow the complete sedimentation of unexfoliated MoS_2 particles. After that, the green colored stable dispersion was pipetted out and dried at 50 °C.

2.2. Nanobattery setup

The sodiation reaction was conducted inside TEM by the nanobattery setup on the Nanofactory holder (Fig. S1), as designed in previous reports [26,32,38]. MoS_2 nanoparticles were pasted on one end of Au rod with conductive epoxy. Sodium metals was sketched by a tungsten
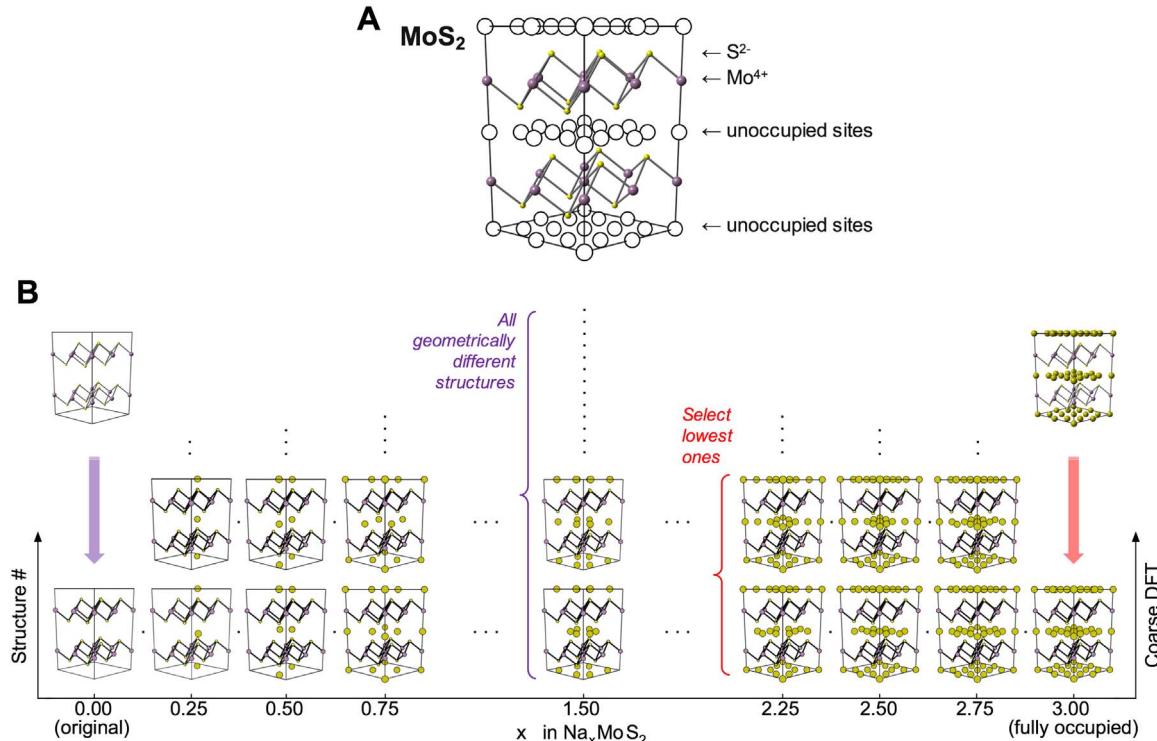
Fig. 1. Search for the metastable structures through the Na-MoS_2 reaction (MoS_2-1T structure, *e.g.*). (A) The normal structure of MoS_2(1T) and unoccupied sites for Na ion insertion (tetrahedral and octahedral sites are exhibited equally). (B) For each stoichiometry, all geometrically different structures are first generated using Enum [42,43]. Low energy structures of specific stoichiometry are determined from the fast energy sampling using coarse DFT calculation settings. Then these low energy structures are further relaxed with strict DFT calculation settings for accurate total energies. The formation energies for these selected structures were then evaluated. Using formation energies obtained, the non-equilibrium Na-MoS_2 convex hull is built. The composition points located on the convex hull then correspond to the identified intermediate phases.
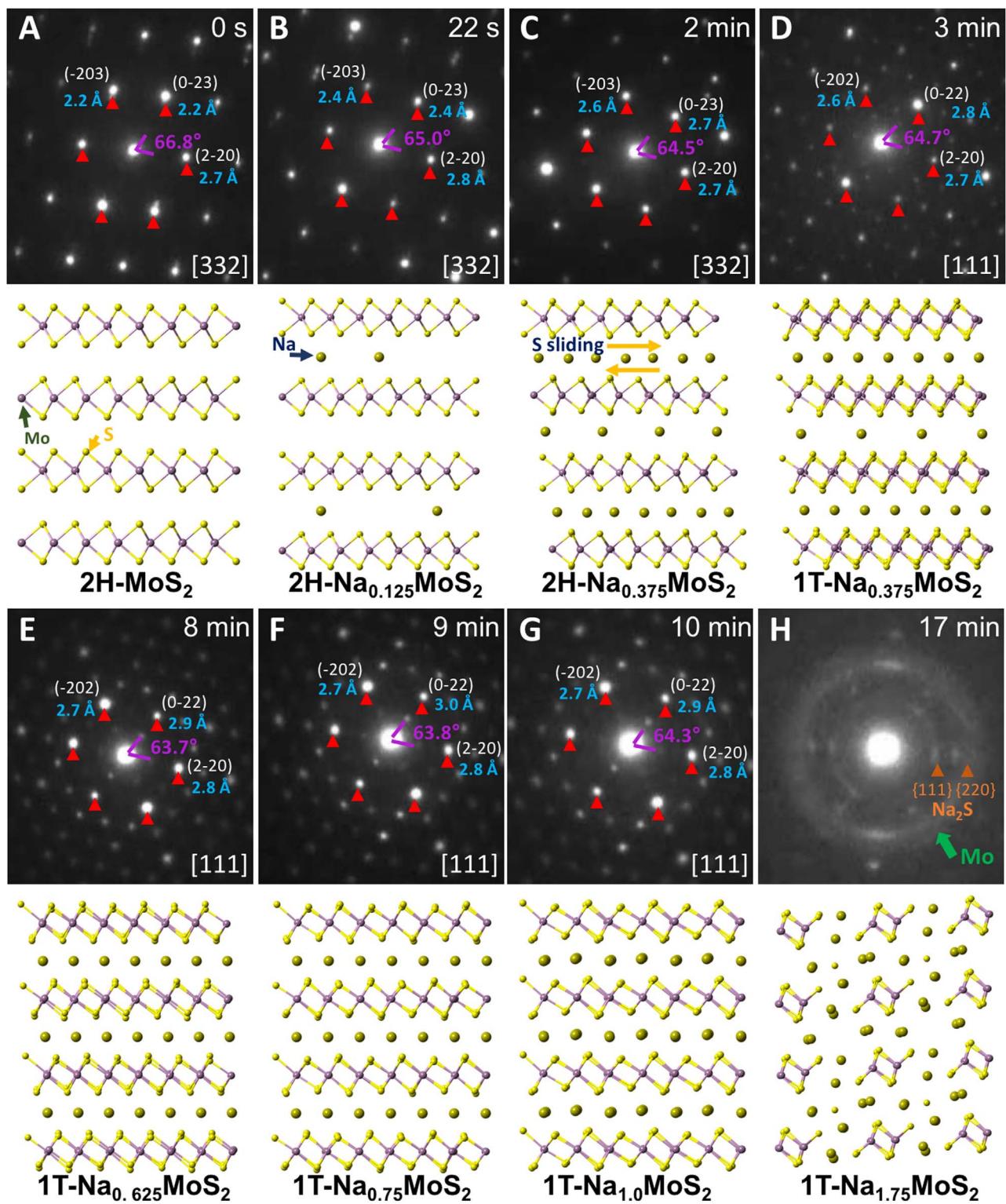
Fig. 2. *In-situ* electron diffraction of Na-intercalation into MoS_2. (A) The starting 2H-MoS_2 is identified to be oriented along the [332] zone axis, along with the illustration of the atomic structure (underneath the pattern). (B)–(H) The indexed diffraction patterns and structural illustrations of Na-ion intercalated structures with Na content from 0.125 to 1.75 (the formula of each crystal is labeled), along with the sodiation, while the sodiation time is marked in each pattern. In each indexed pattern, the measured *d*-spacing of three spots are labeled. When Na content reaches 0.375, a phase transformation from 2H to 1T occurs with the appearance of superlattice spots. When Na content is higher than 1.75, the conversion reaction occurs leading to the formation of Mo and Na_2S.

probe and acted as the counter electrode in the sodium ion batteries. The solid electrolytes used in the *in-situ* TEM experiments consist mainly of Na_2O/NaOH for Na lithiation. In a typical experiment, the porous Na_2O/NaOH film has thickness of about 173–216 nm and high Na-ions' conductivity with Na-ion diffusion activation energy about 0.15 eV [39]. We accurately controlled the counter electrode to touch with the MoS_2 working electrode, then sodiation experiment could be conducted by applying external potential. The microstructure evolutions were studied by *in-situ* electron diffraction patterns in real time with the dosage rate of ~100 e⁻/(nm² S).

2.3. First-principles DFT calculations

First principles density functional theory (DFT) calculations were performed using the Vienna Ab-initio Simulation Package (VASP) [40–43]. Our calculations use the projector augmented wave (PAW) potentials [44], the generalized gradient approximation (GGA) of Perdew-Becke-Ernzerhof (PBE) [45] for exchange-correlation functional, and are spin polarized. We also adopt the vdW-D2 functional to treat exchange and correlation including a self-consistent van der Waals (vdW) correction [46]. We use two different sets of parameters, one for coarse energy configuration sampling, and another for accurate total energy determination of the low energy structures that are determined from the sampling. For coarse sampling calculations, we use a kinetic energy cutoff of 300 eV for the plane wave basis set, and Γ-centered grids of approximately 4000 **k**-points per reciprocal atom. The accurate calculations are performed with a plane-wave basis set cutoff energy of 520 eV, and Γ-centered **k**-meshes with the density of 8000 **k**-points per reciprocal atom.

2.4. Search for the intermediate phases through the Na-MoS$_2$ reaction

To simulate the sodiation process of MoS$_2$, we designed a structure-based method (Fig. 1) to search for intermediate phases by exploring geometrically distinct Na/vacancy configurations on possible insertion sites of MoS$_2$ structures at different compositions (Na/vacancy ratios). We first built models with MoS$_2$ supercells containing 8 Mo atoms and 16 S atoms, which has 8 octahedral and 16 tetrahedral unoccupied sites in which Na$^+$ ions can be inserted (Fig. S2A, B). To investigate the 2 H to 1 T transition, two initial supercell structures corresponding to 2 H and 1 T are created (Fig. S2C, D). Starting from these structures, we inserted the Na atom(s) into the unoccupied octahedral and tetrahedral site(s) for a range of compositions within $0 < x < 3$ for Na$_x$MoS$_2$. For each composition, we generated all symmetrically distinct configurations of Na on these sites using the *Enum* software package developed by Hart et al. [47,48] (Fig. 1). Total energies for these structures were first sampled using coarse DFT calculations with parameters mentioned in Section 2.3. Afterward, the structures at each composition were ranked by the coarse total energies and the lowest three energy structures are further relaxed using more accurate DFT settings. The formation energies for these selected structures were evaluated according to the following reaction: MoS$_2$ + xNa → Na$_x$MoS$_2$. Convex hulls were then built with all formation energies of different stoichiometries. All the intermediate phases were then identified by the compositions on the convex hull. Voltage profiles were calculated using the energetics of the phases on the hull.

3. Results and discussion

The microstructure evolutions of MoS$_2$ have been studied by *in-situ* TEM, especially the *in-situ* electron diffraction. The MoS$_2$ crystals are loaded onto a dedicated *in-situ* TEM holder, and the schematic image about the nanobattery system to study the microstructural evolutions in sodiation is shown in Fig. S1. Selected area electron diffraction (SAED) patterns were collected at a low electron beam dose to monitor the change of the crystalline structure. Unlike the high-resolution electron microscopy, the electron beam can be well spread out and applied to a large area so as to effectively reduce the beam dose. The typical morphology of MoS$_2$ flakes being studied is shown in Fig. S3, where the size of the flake is as large as few hundred nanometers. Video S1 shows the recorded SAED patterns along with the sodiation process last for 56 min. The 2H-MoS$_2$ crystal prior to Na-intercalation is identified to be oriented along the [332] zone axis; its SAED pattern is shown in Fig. 2A and an illustration of the 2H-MoS$_2$ structure showing S-Mo-S layers in Fig. 1A. In the early stage of sodiation, the {023} diffraction spots moved toward the (000) spot when the

intercalated Na content increased. The {023} *d*-spacing increased from 2.2 Å to 2.4 Å in 22 s′ sodiation (Fig. 2B); and then to 2.7 Å (Fig. 2C) in about 2 min′ sodiation.

Supplementary material related to this article can be found online at doi:10.1016/j.nanoen.2017.05.055.

By using a combination of electron diffraction and DFT calculations, we can identify the content of Na in the intermediate phases. The structural evolution was studied by a series of electron diffraction patterns, and the same phase transformation process was calculated by DFT. The simulated diffraction patterns were then calculated with the structural models generated by DFT and compared to the experimental ones, and the comparison allows us to identify possible intermediate phases. This method allows us to identify the intermediate phases, their compositions (x in Na$_x$MoS$_2$), as well as the voltages.

With DFT calculations as described in Section 2 (Fig. 1, Section S1) and SAED patterns simulations (Fig. S4), the phases in the first stage of sodiation can be identified as 2H-Na$_{0.125}$MoS$_2$ and 2H-Na$_{0.375}$MoS$_2$, respectively. In this stage, Na-ions are randomly intercalated into the unoccupied inter-layer sites as illustrated in Fig. 2B and Fig. 2C, respectively. The 2H-MoS$_2$ lattice slightly expands due to random insertion of the Na-ion and electron. The lattice parameters of 2H-MoS$_2$, 2H-Na$_{0.125}$MoS$_2$ and 2H-Na$_{0.375}$MoS$_2$ are listed in Table S1 and the comparison of the observed and calculated *d*-spacing of the {023} and {220} lattice planes is shown in Fig. 3. The 2H-type lattice in which Mo and S are bonded by strong covalent bonds forming trigonal prism (as shown Fig. S2) remains stable when the number of intercalated Na-ions (electrons) is less than 0.35 per MoS$_2$ formula unit. The critical content of 0.375 has been predicted by previous DFT calculations [49–51] and confirmed by this study (Fig. S5). The phase transformation from 2H- to 1T-MoS$_2$, induced by sodium ion electrochemical and chemical intercalation, has also been confirmed by XPS as shown in Fig. S8 and discussed in Section S3.

After sodiation for about 3-min, extra diffraction spots appeared in the pattern as shown in Fig. 2D. This is the sign of the Na-ions ordering in the structure, meaning that Na-ions occupy octahedral (S-prism) inter-layered sites in an ordered pattern, unlike the random distribution in these sites at the beginning of sodiation. Interestingly, we found that such a disordered to ordered structural transformation occurs coincidently with the phase transformation from 2H-MoS$_2$ to 1T-MoS$_2$, as supported by DFT calculations and SAED patterns simulation and
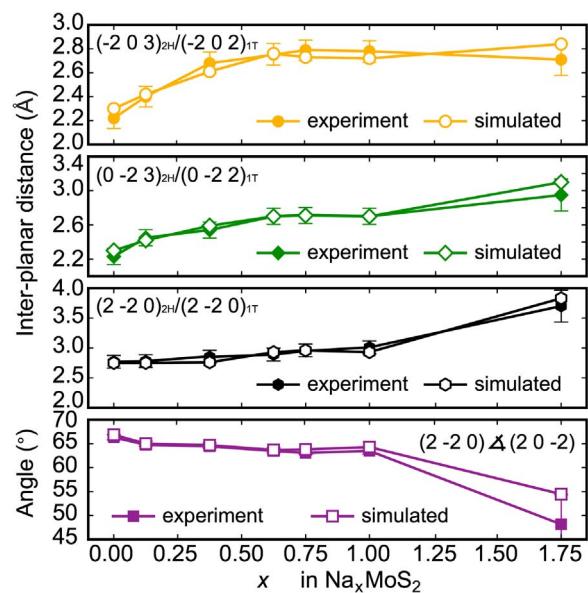
Fig. 3. Comparison of calculated and experimental spacing of the lattice plane (–2 0 3)_2H, (–2 0 2)_1T, (0 –2 3)_2H, (0 –2 2)_1T, (2 –2 0)_2H and (2 –2 0)_1T, and angles between the (2 –2 0) and (2 0 –2) for all the intermediate phases during the sodiation of the MoS$_2$ nano particle.
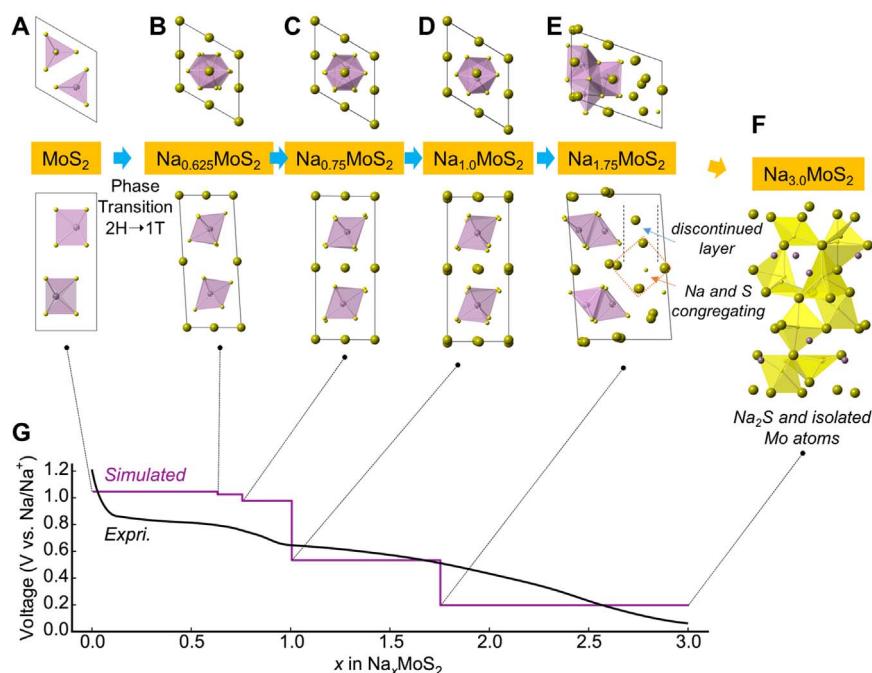
Fig. 4. Electrochemical sodiation process of MoS_2. Start from the original 2H MoS_2 structure (A, $x = 0$), the sodiation proceeds through a phase transition from 2H to 1T structure (B, $x = 0.625$) by S ion shifting and reordering. Further sodiation occurs *via* two intermediate phases (C, $x = 0.75$), (D, $x = 1.0$) by Na ion ordering with intact Mo and S backbones. The Mo-S layers start to collapse when more than 1.5 Na ions inserted (E, $x = 1.75$). Na ion intercalation stops after that and the sodiation reaction switches to the conversion style with the final phase ($x = 3.0$, F) featured with Na_2S and isolated Mo atoms. (G) Simulated voltage profile of MoS_2 through the intermediate phases, compared to experimental voltage profile adapted from Ref. [12].

comparison. When the Na-ion ordering occurs differently in alternate intercalation layers (as shown in Fig. S2), the phase transformation from 2H to 1T is triggered, and lowers the overall energy, as indicated by DFT calculations. At the same time, the 2H to 1T phase transformation is enabled by the sliding and ordering of the S-Mo-S layers. Due to slight deformation of the lattice from 2H to 1T, the 2H-[332] zone axis is very closed to the 1T-[111] axis.

During further sodiation (from 3 min to about 11 min), the extra diffraction spots due to ordered 1T-Na_xMoS_2 structures gain higher and higher intensity, while the *d*-spacing of the {202} reflections increased when more and more Na-ion and electrons intercalated into the structure. Several intermediate structures are identified as shown in Fig. 2D–H, namely 1T-$Na_{0.375}MoS_2$ (Fig. 2D), 1T-$Na_{0.625}MoS_2$ (Fig. 2E), 1T-$Na_{0.75}MoS_2$ (Fig. 2F), 1T-$Na_{1.0}MoS_2$ (Fig. 2G) and 1T-
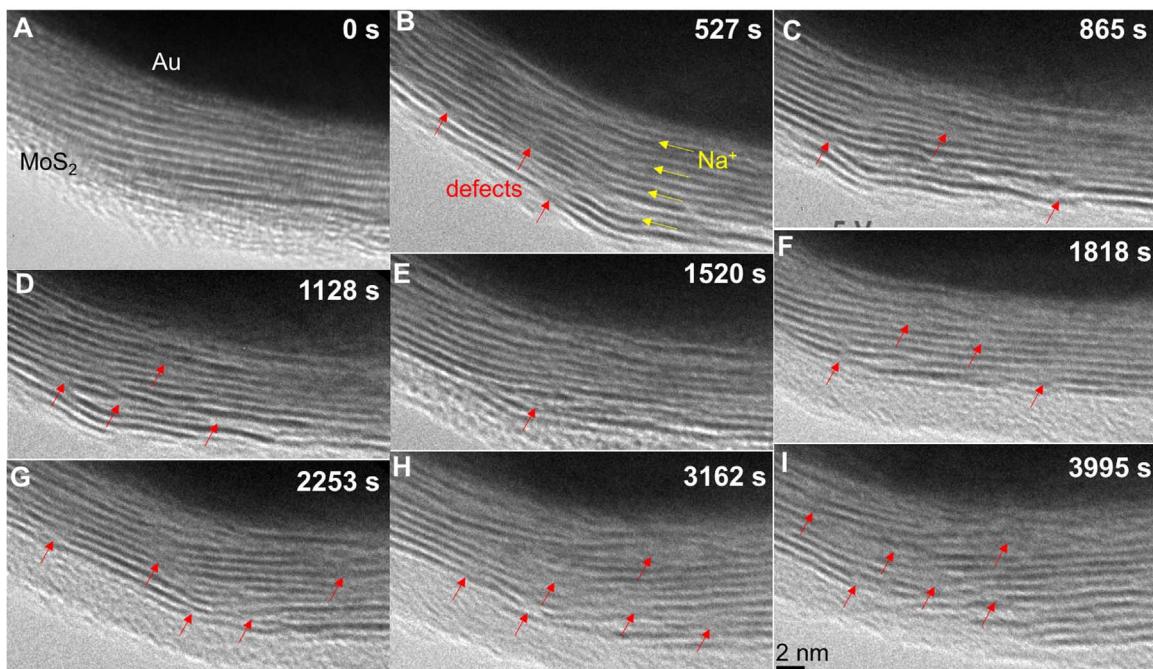
Fig. 5. Anisotropic diffusion of Na-ions and generation of defects in sodiation. (A) About 13 layers of MoS_2 coated on the Au particle before sodiation. The lattice fringes can thus be identified as the MoS_2-{001} lattice plane. (B)–(D) *in-situ* TEM images of the Na-intercalated MoS_2 at different reaction time as marked. Na-ions are mainly diffused along the {001} layers as marked by yellow arrowheads. Defects, as labeled by red arrowheads, are generated at the boundaries with phases having different Na-content. (For interpretation of the references to color in this figure legend, the reader is referred to the web version of this article.).

$Na_{1.75}MoS_2$ (Fig. 2H). When the number of intercalated Na is less than 1, Na-ions occupy the octahedral sites. Here a portion of the Mo^{4+}-ions have been reduced to Mo^{3+}, which introduces a small deformation in the Mo-S octahedron (as shown in Fig. 4). When there are more than 1 Na-ions being intercalated, the Na ions start to occupy the empty tetrahedral sites. When there is 1 Na-ion intercalated, all of the Mo-ions in S-Mo-S layer have been reduced to Mo^{3+} and the resulting structural arrangement is isostructural with the known $LiMoS_2$ compound (Fig. S6) [52,53]. With further Na-intercalation, some of the Mo^{3+} is further reduced to Mo^{2+}. The reduction of the Mo-ions will expand the Mo-S octahedron, pushing S^{2-} out toward the Na^+.

Further sodiation (beyond 1.75 Na intercalated per formula unit of MoS_2) causes phase separation and collapse of the MoS_2-layered structure. A wide and diffuse ring emerges in the diffraction pattern shown in Fig. 2H, implying a disordered, amorphous-like structure formed to replace the ordered and layered structures based on the MoS_2 backbone. A careful analysis of the diffraction pattern in Fig. 2H confirms the formation of Na_2S nanocrystals and Mo metal nanoclusters. With the further insertion of electrons, the Mo^{2+}-ions are further reduced to metallic Mo, extruded from the S-Mo-S polyhedral and aggregating together to form small clusters. Meanwhile, the S-Na bonds form leading to the formation of Na_2S nanocrystals.

There are several stable phases (as predicted to be on the Na-MoS_2 convex hull, Fig. S6) identified by electron diffraction and DFT calculations, such as $Na_{0.625}MoS_2$, $Na_{0.75}MoS_2$, $Na_{1.0}MoS_2$, $Na_{1.75}MoS_2$. The voltage profile calculated based on the stable intermediate phases is drawn in Fig. 4, which matches the experimental voltages much better than the corresponding calculated voltages without the intermediate phases [54]. It is interesting to note that the intermediate phases with a high Na contents ($0.625 < x < 1.75$) are thermodynamically stable ones. On the other hand, at the beginning of the intercalation, reactions with low Na contents ($0.125 < x < 0.5$) involve phases which are mostly metastable according to the DFT calculations. This distinction can be understood in terms of the role of reaction kinetics. In the early stages of the reaction, the metastable phases have insufficient time to relax to their stable counterparts since the initial insertion of Na-ions has fast kinetics compared to Mo and S ions as observed in previously studies [55,56]. The metastable phases would thus dominate in early stages of the Na-MoS_2 reaction when the localized charge/discharge processes occur at high speed.

We examine the Na-ion diffusion and intercalation into the MoS_2 crystal during the sodiation reaction close to the [100] direction. As shown in Fig. 5 and Video S2, the Mo-S-Mo layers have the contrast of dark fringes in the images when they are at the edge-on orientation. In this sample, MoS_2 layers are coated on the surfaces of Au nanoparticle. The measured d-spacing of each layer is about 0.595 ± 0.3 nm, corresponding to the {001} lattice planes of the MoS_2 crystal. Along with the intercalation of the Na, the {001} layers expanded, as shown in Fig. 5A–D. Meanwhile, at the interface of the Na-rich MoS_2 and original MoS_2 phases, the layers are broken and shifted due to a large expansion in the Na-rich side leading to the creation of many "anti-phase" boundary like defects as marked by the red arrows in Fig. 5B–D. The repeated occurrence of such anti-phase boundary defects will eventfully cut the layers into many small fragments. The diffusion of the Na-ions is mainly along the interlayer space at the initial stage of sodiation as labeled by the yellow arrows. However, once the Na-intercalated MoS_2 become small fragments with a large density of planar defects, it is possible for the diffusion of Na-ions to cross the layers. The intercalation of Na-ions into MoS_2 involves not only crystalline phase transformations, but also is accompanied by the generation and motion of the defects in the boundaries. These defects create small crystalline domains which will prompt the transition from intercalation reaction to conversion reaction for high Na contents. The planar defects are induced by the large in-plane misfit stresses due to sodiation/desodiation. We suggest that these defects are a kind of structural precursor to the electrochemically driven conversion reac-

tion [57]. These defects, such as planar defects, twin boundaries, misfit dislocations, vacancies, *etc.*, have been identified as a facile pathway for diffusion, facilitating alkali ion insertion into the electrode materials [58–60]. Additionally, theoretical calculations, such as DFT and molecular dynamics simulations, show the defects can decrease the alkali ion migration barriers and increase the diffusion coefficients [61], and enhance the energy storage capacity of the electrodes [62].

Supplementary material related to this article can be found online at doi:10.1016/j.nanoen.2017.05.055.

4. Conclusions

In summary, several stable/metastable phases ($Na_{0.375}MoS_2$, $Na_{0.625}MoS_2$, $Na_{0.75}MoS_2$, $Na_{1.0}MoS_2$, $Na_{1.75}MoS_2$) have been identified in the early stages of sodiation in nanostructured MoS_2 crystals. The nano-MoS_2 crystal can host up to 1.75 Na per unit formula before the layered structure collapses. Along with the insertion of Na-ions into MoS_2, the Mo^{4+} is reduced gradually to Mo^{3+}, Mo^{2+} and eventually Mo^0 atoms to accommodate the added electrons. We confirm a phase transformation from 2H- to 1T MoS_2 when the Na content is 0.375, along with Na-ion ordering in the 1T structure. The diffusion of Na-ions is quite anisotropic, fast diffusion along the S-Mo-S layers and almost no diffusion cross the layer. Many planar defects are generated during sodiation, which prompts the transition from intercalation reaction to conversion reaction when the Na content becomes high. This study provides insight to understand the sodiation transformations and kinetics in a typical layered transition-metal dichalcogenide structure, which should be helpful in the future design of advanced sodium ion batteries.

Acknowledgements

Appendix A. Supplementary material

Supplementary data associated with this article can be found in the online version at doi:10.1016/j.nanoen.2017.05.055.

References

[1] D. Kim, S.H. Kang, M. Slater, S. Rood, J.T. Vaughey, N. Karan, M. Balasubramanian, C.S. Johnson, Adv. Energy Mater. 1 (2011) 333–336.

[2] S. Komaba, W. Murata, T. Ishikawa, N. Yabuuchi, T. Ozeki, T. Nakayama, A. Ogata, K. Gotoh, K. Fujiwara, Adv. Funct. Mater. 21 (2011) 3859–3867.
[3] D. Larcher, J. Tarascon, Nat. Chem. 7 (2014) 19–29.
[4] V. Palomares, P. Serras, I. Villaluenga, K.B. Hueso, J. Carretero-González, T. Rojo, Energy Environ. Sci. 5 (2012) 5884–5901.
[5] J. Xiao, D. Choi, L. Cosimbescu, P. Koech, J. Liu, J.P. Lemmon, Chem. Mater. 22 (2010) 4522–4524.
[6] J. Wang, C. Luo, T. Gao, A. Langrock, A.C. Mignerey, C. Wang, Small 11 (2015) 473–481.
[7] C. Julien, S.I. Saikh, G.A. Nazri, Mater. Sci. Eng. B 15 (1992) 73–77.
[8] L. David, R. Bhandavat, G. Singh, ACS Nano 8 (2014) 1759–1770.
[9] Y.-X. Wang, K.H. Seng, S.-L. Chou, J.-Z. Wang, Z. Guo, D. Wexler, H.-K. Liu, S.-X. Dou, Chem. Commun. 50 (2014) 10730–10733.
[10] L. Wang, Z. Xu, W. Wang, X. Bai, J. Am. Chem. Soc. 136 (2014) 6693–6697.
[11] P. Gao, L. Wang, Y. Zhang, Y. Huang, K. Liu, ACS Nano 9 (2015) 11296–11301.
[12] Y. Liang, H.D. Yoo, Y. Li, J. Shuai, H.A. Calderon, F.C. Robles Hernandez, L.C. Grabow, Y. Yao, Nano Lett. 15 (2015) 2194–2202.
[13] R. Somoano, V. Hadek, A. Rembaum, J. Chem. Phys. 58 (1973) 697–701.
[14] E. Benavente, M.A. Santa Ana, F. Mendizábal, G. González, Coord. Chem. Rev. 224 (2002) 87–109.
[15] H. Hwang, H. Kim, J. Cho, Nano Lett. 11 (2011) 4826–4830.
[16] T.S. Sahu, Q. Li, J. Wu, V.P. Dravid, S. Mitra, J. Mater. Chem. A 5 (2017) 355–363.
[17] X. Wang, X. Shen, Z. Wang, R. Yu, L. Chen, ACS Nano 8 (2014) 11394–11400.
[18] R. Bissessur, M.G. Kanatzidis, J.L. Schindler, C.R. Kannewurf, Chem. Commun. 20 (1993) 1582–1585.
[19] F. Wypych, R. Schollhorn, Chem. Commun. 19 (1992) 1386–1388.
[20] L.F. Mattheiss, Phys. Rev. B 8 (1973) 3719–3740.
[21] C. Julien, MRS Bull. 293 (1992) 411.
[22] G.S. Bang, K.W. Nam, J.Y. Kim, J. Shin, J.W. Choi, S.-Y. Choi, ACS Appl. Mater. Interfaces 6 (2014) 7084–7089.
[23] Q. Li, P. Wang, Q. Feng, M. Mao, J. Liu, S.X. Mao, H. Wang, Chem. Mater. 26 (2014) 4102–4108.
[24] A. Nie, L.-Y. Gan, Y. Cheng, Q. Li, Y. Yuan, F. Mashayek, H. Wang, R. Klie, U. Schwingenschlogl, R. Shahbazian-Yassar, Nano Lett. 15 (2014) 610–615.
[25] A. Nie, L.-Y. Gan, Y. Cheng, X. Tao, Y. Yuan, S. Sharifi-Asl, K. He, H. Asayesh-Ardakani, V. Vasiraju, J. Lu, Adv. Funct. Mater. 26 (2015) 543–552.
[26] X.H. Liu, J.Y. Huang, Energy Environ. Sci. 4 (2011) 3844–3860.
[27] C.M. Wang, X.L. Li, Z.G. Wang, W. Xu, J. Liu, F. Gao, L. Kovarik, J.G. Zhang, J. Howe, D.J. Burton, Z.Y. Liu, X.C. Xiao, S. Thevuthasan, D.R. Baer, Nano Lett. 12 (2012) 1624–1632.
[28] L. Luo, B. Zhao, B. Xiang, C.-M. Wang, ACS Nano 10 (2015) 1249–1255.
[29] K. He, F. Lin, Y. Zhu, X. Yu, J. Li, R. Lin, D. Nordlund, T.-C. Weng, R.M. Richards, X.-Q. Yang, M. Doeff, E.A. Stach, Y. Mo, H.L. Xin, D. Su, Nano Lett. 15 (2015) 5755–5763.
[30] K. He, S. Zhang, J. Li, X. Yu, Q. Meng, Y. Zhu, E. Hu, K. Sun, H. Yun, X.-Q. Yang, Nat. Commun. 7 (2016) 11441–11449.
[31] K. He, Y. Zhou, P. Gao, L. Wang, N. Pereira, G.G. Amatucci, K.-W. Nam, X.-Q. Yang, Y. Zhu, F. Wang, ACS Nano 8 (2014) 7251–7259.
[32] J.Y. Huang, L. Zhong, C.M. Wang, J.P. Sullivan, W. Xu, L.Q. Zhang, S.X. Mao, N.S. Hudak, X.H. Liu, A. Subramanian, Science 330 (2010) 1515–1520.
[33] M.T. McDowell, S.W. Lee, J.T. Harris, B.A. Korgel, C.M. Wang, W.D. Nix, Y. Cui, Nano Lett. 13 (2013) 758–764.
[34] M.M. Thackeray, C. Wolverton, E.D. Isaacs, Energy Environ. Sci. 5 (2012) 7854–7863.
[35] M. Aykol, S. Kim, V.I. Hegde, D. Snydacker, Z. Lu, S. Hao, S. Kirklin, D. Morgan, C. Wolverton, Nat. Commun. 7 (2016) 13779–13790.
[36] S. Kirklin, B. Meredig, C. Wolverton, Adv. Energy Mater. 3 (2013) 252–262.
[37] H. Bin, Z. Yao, S. Zhu, C. Zhu, H. Pan, Z. Chen, C. Wolverton, D. Zhang, J. Alloy. Compd. 695 (2017) 1223–1230.
[38] M.T. McDowell, S.W. Lee, C. Wang, W.D. Nix, Y. Cui, Adv. Mater. 24 (2012) 6034–6041.
[39] Q. Li, H. Liu, Z. Yao, J. Cheng, T. Li, Y. Li, C. Wolverton, J. Wu, V.P. Dravid, ACS Nano 10 (2016) 8788–8795.
[40] G. Kresse, J. Hafner, Phys. Rev. B 47 (1993) 558–561.
[41] G. Kresse, J. Hafner, Phys. Rev. B 49 (1994) 14251–14271.
[42] G. Kresse, J. Furthmüller, Comput. Mater. Sci. 6 (1996) 15–50.
[43] G. Kresse, J. Furthmüller, Phys. Rev. B 54 (1996) 11169–11186.
[44] P.E. Blöchl, Phys. Rev. B 50 (1994) 17953–17979.
[45] J.P. Perdew, M. Ernzerhof, K. Burke, J. Chem. Phys. 105 (1996) 9982–9985.
[46] H. Peelaers, C.G. Van de Walle, J. Phys.: Condens. Matter 26 (2014) 305502–305508.
[47] G.L. Hart, L.J. Nelson, R.W. Forcade, Comput. Mater. Sci. 59 (2012) 101–107.
[48] G.L. Hart, R.W. Forcade, Phys. Rev. B 77 (2008) 224115–224126.
[49] L. Yadgarov, R. Rosentsveig, G. Leitus, A. Albu-Yaron, A. Moshkovich, V. Perfilyev, R. Vasic, A.I. Frenkel, A.N. Enyashin, G. Seifert, Angew. Chem. Int. Ed. 51 (2012) 1148–1151.
[50] A.N. Enyashin, G. Seifert, Comput. Theor. Chem. 999 (2012) 13–20.
[51] M. Mortazavi, C. Wang, J. Deng, V.B. Shenoy, N.V. Medhekar, J. Power Sources 268 (2014) 279–286.
[52] X. Rocquefelte, I. Bouessay, F. Boucher, P. Gressier, G. Ouvrard, J. Solid State Chem. 175 (2003) 380–383.
[53] V. Petkov, S. Billinge, P. Larson, S. Mahanti, T. Vogt, K. Rangan, M.G. Kanatzidis, Phys. Rev. B 65 (2002) 921051–921054.
[54] Y.-X. Wang, K.H. Seng, S.-L. Chou, J.-Z. Wang, Z. Guo, D. Wexler, H.-K. Liu, S.-X. Dou, Chem. Commun. 50 (2014) 10730–10733.
[55] D. Chang, M.-H. Chen, A. Van der Ven, Chem. Mater. 27 (2015) 7593–7600.
[56] H.-C. Yu, C. Ling, J. Bhattacharya, J.C. Thomas, K. Thorntona, A. Van der Ven, Energy Environ. Sci. 7 (2014) 1760–1768.
[57] J.Y. Huang, L. Zhong, C.M. Wang, J.P. Sullivan, W. Xu, L.Q. Zhang, S.X. Mao, N.S. Hudak, X.H. Liu, A. Subramanian, Science 330 (2010) 1515–1520.
[58] A. Nie, L.-Y. Gan, Y. Cheng, H. Asayesh-Ardakani, Q. Li, C. Dong, R. Tao, F. Mashayek, H.-T. Wang, U. Schwingenschlögl, ACS Nano 7 (2013) 6203–6211.
[59] M. Legros, G. Dehm, E. Arzt, T.J. Balk, Science 319 (2008) 1646–1649.
[60] A. Nie, L.-Y. Gan, Y. Cheng, Q. Li, Y. Yuan, F. Mashayek, H. Wang, R. Klie, U. Schwingenschlogl, R. Shahbazian-Yassar, Nano Lett. 15 (2014) 610–615.
[61] P.M. Panchmatia, A.R. Armstrong, P.G. Bruce, M.S. Islam, Phys. Chem. Chem. Phys. 16 (2014) 21114–21118.
[62] X. Sun, Z. Wang, Y.Q. Fu, Sci. Rep. 5 (2015) 18712–18720.

Qianqian Li received her Ph.D. from Zhejiang University in solid mechanics. She now is postdoctoral research assistant in NUANCE, Department of Materials Science and Engineering, at Northwestern University, Evanston, IL. Her research area of interest includes *in-situ* transmission electron microscopy (TEM) and other characterization tools, energy storage behaviors of electrodes for rechargeable batteries and supercapacitor, and synthesis and modification of functional materials.

Zhenpeng Yao is currently a research assistant and Ph.D. student in Department of Materials Science and Engineering at the Northwestern University. He earned his M.S. degree from the Department of Mechanical Engineering at Shanghai Jiao Tong University, China. His research interests include first-principle studies on novel electrode materials and solid state electrolytes for rechargeable lithium and sodium-ion batteries.

Dr. Jinsong Wu is currently a research associate professor in Department of Materials Science and Engineering at the Northwestern University and TEM facility manager in the NUANCE center. He earned his Ph.D. degree from the Department of Materials Science and Engineering at Dalian University of Technology, China. As an award winning microscopist, Dr. Wu's research interests include transmission electron microscopy, electron tomography, *in-situ* transmission electron microscopy and nanomaterials for energy storage.

Sagar Mitra is Associate Professor of Department of Energy Science and Engineering at Indian Institute of Technology Bombay, Mumbai India. He is currently leading the battery research team in National Center for Solar Photovoltaic Research and Education (funded by Ministry of New and Renewable Energy, Govt. of India) at IIT Bombay and his current research mainly focused on advanced materials and technology development for different energy storage applications, particularly in lithium-ion batteries and sodium-ion batteries.

Shiqiang Hao received his Ph.D. in condensed matter physics from Tsinghua University in 2002. He is currently a senior research associate at Northwestern University. His computational research covers a wide range of functional materials for alternative energies and sustainability. His recent work involves high efficiency thermoelectrics, two-dimensional layered materials, and Li ion battery materials.

Chris Wolverton is a professor in the Materials Science Department at Northwestern University. Before joining the faculty, he worked at the Research and Innovation Center at Ford Motor Company. He received his BS degree in Physics from the University of Texas at Austin and his Ph.D. degree in Physics from the University of California at Berkeley, and performed postdoctoral work at the National Renewable Energy Laboratory (NREL). His research interests include computational studies of a variety of energy-efficient and environmentally friendly materials *via* first-principles atomistic and multiscale calculations. Professor Wolverton is a Fellow of the American Physical Society.

Tuhin Subhra Sahu received his master's degree from Indian School of Mines (ISM) Dhanbad (2013). After that he worked as a research assistant under the supervision of Dr. Sagar Mitra at Indian Institute of Technology (IIT) Bombay (2014–2016). He is currently pursuing his Ph.D. degree at Center for Clean Energy Technology, University of Technology Sydney. His main research interest is exfoliation of two-dimensional (2D) layered materials as anodes for sodium-ion batteries and fabrication of electro-materials for cathode applications in lithium-sulfur batteries.

Prof. Vinayak P. Dravid is the Abraham Harris Chaired Professor of Materials Science & Engineering at and the founding director of the NU*ANCE* Center at Northwestern University. He received his Bachelor of Technology (B. Tech.) in Metallurgical Engineering from IIT Bombay, India; and PhD in Materials Science and Engineering from Lehigh University. He has a diverse research portfolio encompassing advanced microscopy, nanotechnology, technology strategy, energy policy and emerging educational paradigms.

Yuan Li received his BS (in 2009) and MS (in 2011) in Metallurgical Engineering from Central South University, China. He completed his PhD (in 2015) in Materials Science from The University of Alabama, USA. He is currently a postdoctoral research associate in Northwestern University. His research interests focus on developing novel heterostructured nanomaterials for optical and electronic sensors.